The Astrophysical Journal, 821:65 (12pp), 2016 April 10 doi:10.3847/0004-637X/821/1/65

EVIDENCE FOR REFLECTED LIGHT FROM THE MOST ECCENTRIC EXOPLANET KNOWN

Stephen R. Kane[1], Robert A. Wittenmyer[2,3,4], Natalie R. Hinkel[1,5], Arpita Roy[6,7], Suvrath Mahadevan[6,7], Diana Dragomir[8], Jaymie M. Matthews[9], Gregory W. Henry[10], Abhijit Chakraborty[11], Tabetha S. Boyajian[12], Jason T. Wright[6,7], David R. Ciardi[13], Debra A. Fischer[12], R. Paul Butler[14], C. G. Tinney[2,3], Brad D. Carter[4], Hugh R. A. Jones[15], Jeremy Bailey[2,3], and Simon J. O'Toole[16]
[1] Department of Physics & Astronomy, San Francisco State University, 1600 Holloway Avenue, San Francisco, CA 94132, USA; skane@sfsu.edu
[2] School of Physics, University of New South Wales, Sydney, NSW 2052, Australia
[3] Australian Center for Astrobiology, University of New South Wales, Sydney, NSW 2052, Australia
[4] Computational Engineering and Science Research Centre, University of Southern Queensland, Toowoomba, Queensland 4350, Australia
[5] School of Earth & Space Exploration, Arizona State University, Tempe, AZ 85287, USA
[6] Department of Astronomy and Astrophysics, Pennsylvania State University, 525 Davey Laboratory, University Park, PA 16802, USA
[7] Center for Exoplanets & Habitable Worlds, Pennsylvania State University, 525 Davey Laboratory, University Park, PA 16802, USA
[8] Las Cumbres Observatory Global Telescope Network, 6740 Cortona Drive, Suite 102, Goleta, CA 93117, USA
[9] Department of Physics and Astronomy, University of British Columbia, Vancouver, BC V6T1Z1, Canada
[10] Center of Excellence in Information Systems, Tennessee State University, 3500 John A. Merritt Boulevard, Box 9501, Nashville, TN 37209, USA
[11] Division of Astronomy, Physical Research Laboratory, Navrangpura, Ahmedabad 380009, India
[12] Department of Astronomy, Yale University, New Haven, CT 06511, USA
[13] NASA Exoplanet Science Institute, Caltech, MS 100-22, 770 South Wilson Avenue, Pasadena, CA 91125, USA
[14] Department of Terrestrial Magnetism, Carnegie Institution of Washington, 5241 Broad Branch Road, NW, Washington, DC 20015-1305, USA
[15] University of Hertfordshire, Centre for Astrophysics Research, Science and Technology Research Institute, College Lane, AL10 9AB, Hatfield, UK
[16] Australian Astronomical Observatory, P.O. Box 915, North Ryde, NSW 1670, Australia
Received 2015 November 27; accepted 2016 February 26; published 2016 April 11

ABSTRACT

Planets in highly eccentric orbits form a class of objects not seen within our solar system. The most extreme case known among these objects is the planet orbiting HD 20782, with an orbital period of 597 days and an eccentricity of 0.96. Here we present new data and analysis for this system as part of the Transit Ephemeris Refinement and Monitoring Survey. We obtained CHIRON spectra to perform an independent estimation of the fundamental stellar parameters. New radial velocities from Anglo-Australian Telescope and PARAS observations during periastron passage greatly improve our knowledge of the eccentric nature of the orbit. The combined analysis of our Keplerian orbital and *Hipparcos* astrometry show that the inclination of the planetary orbit is $>1\overset{\circ}{.}22$, ruling out stellar masses for the companion. Our long-term robotic photometry show that the star is extremely stable over long timescales. Photometric monitoring of the star during predicted transit and periastron times using *Microvariability and Oscillations of STars* rule out a transit of the planet and reveal evidence of phase variations during periastron. These possible photometric phase variations may be caused by reflected light from the planet's atmosphere and the dramatic change in star–planet separation surrounding the periastron passage.

Key words: planetary systems – stars: individual (HD 20782) – techniques: photometric – techniques: radial velocities

1. INTRODUCTION

Exoplanetary system architectures have revealed numerous surprises since the first exoplanets were discovered. One of the earliest surprises was the discovery of exoplanets in highly eccentric orbits, for which there is no analog in the Solar System. These eccentric orbits were discovered for giant planets, such as HD 114762b (Latham et al. 1989; Kane et al. 2011) and 70 Vir b (Marcy & Butler 1996; Kane et al. 2015) with eccentricities of 0.33 and 0.40 respectively. Since those early discoveries, eccentric planets have presented a significant challenge for formation theories to account for the components of planet–planet scattering (Chatterjee et al. 2008; Petrovich et al. 2014) and tidal circularization (Pont et al. 2011). Such planets tend to be discovered with the radial velocity (RV) technique since the observations are able to sample the entire Keplerian planetary orbit. Subsequent investigations of the eccentricity distribution of planetary orbits that take *Kepler* transiting exoplanet discoveries into account show that small planets in multi-planet systems are more likely to have low eccentricities (Kane et al. 2012; Van Eylen & Albrecht 2015). The discovery and characterization of eccentric orbits is an ongoing effort to understand the evolutionary history of these fascinating systems.

A particularly eccentric exoplanet was discovered by Jones et al. (2006) orbiting the star HD 20782. With a minimum mass twice that of Jupiter and an orbital period of 597 days, the planet is typical of high-eccentricity planets. The orbit was further revised by O'Toole et al. (2009) and shown to have an eccentricity as high as 0.97, making it the highest eccentricity exoplanet yet discovered. However, data during periastron passage is difficult to obtain for such systems since the RV variation predominantly occurs during a very small fraction of the orbital phase. The star continued to be monitored by the Transit Ephemeris Refinement and Monitoring Survey (TERMS) to improve the orbital parameters of the system (Kane et al. 2009). Such orbital refinement may be used to predict and observe events that occur during particular periods of the orbit, such as planetary transits (Kane & von Braun 2008) or phase variations (Kane & Gelino 2010).

Here we present new results for the HD 20782 system, including RVs that sample several periastron passages and establish the planet as the most eccentric known exoplanet.

Follow-up photometry from both ground-based and space-based telescopes rule out a transit of the planet and show evidence of phase variations due to reflected light from the planet close to periastron passage. Section 2 provides background information and discusses the science motivation for studying the system. Section 3 presents analysis of new CHIRON spectra and the resulting fundamental parameters of the host star as well as stellar abundances. New RV data are combined with those published in Section 4 and a new Keplerian orbit for the planet is produced. Section 5 describes the use of *Hipparcos* astrometry to constrain the orbital inclination of the planet. Section 6 discusses the transit prospects for the system and the effects of both orbital eccentricity and inclination. Section 7 presents the ground-based photometry and an estimate of the stellar rotation period. Data from *Microvariability and Oscillations of STars* (*MOST*) are used during the transit/periastron window to rule out a transit and also reveal the potential presence of a reflected light signature of the planet as it passes through periastron passage. We discuss future observing opportunities and make concluding remarks in Section 8.

2. SCIENCE MOTIVATION

The eccentricity distribution of exoplanets has a well-defined shape whereby the orbits diverge from circular beyond a semimajor axis of ~0.1 au (Butler et al. 2006; Kane 2013), inside of which tidal circularization tends to force low eccentricity (Goldreich & Soter 1966; Pont et al. 2011). The observed eccentricity distribution is a clear indicator of formation processes that are dependent upon initial system architectures, in particular planet–planet scattering. Wide binaries may inadvertantly create a more suitable environment for the formation of highly eccentric planetary orbits through gravitational perturbations from the companion star and the triggering of planetary ejections (Kaib et al. 2013).

HD 20782 is part of a wide binary with HD 20781 having a projected separation of 9000 au, recently described by Mack et al. (2014). The known planet orbiting HD 20782 lies at the very top of the exoplanet eccentricity distribution, though RV measurements during the crucial periastron passage were relatively rare. The extreme nature of the planet's orbital eccentricity may be seen in Figure 1, where the orbit is described using our expanded data set (see Section 4).

Our further investigations of this system are primarily motivated by a better characterization of the planetary orbit and performing follow-up observations at key orbital phases that can help to understand the nature of the planet. It is also important to establish that the secondary object is indeed a planet since a face-on orbital orientation would make it consistent with the eccentricity distribution of spectroscopic binaries (Meibom & Mathieau 2005; Mazeh 2008).

The orbital orientation depicted in Figure 1 shows that the star–planet separation along the line of sight to the observer is quite small, despite the ~18 month orbital period. This yields a relatively high transit probability equivalent to that of a hot Jupiter (see Section 6). Thus a primary motivation for follow-up observations is the possible detection of a planetary transit for a long-period eccentric planet (Kane & von Braun 2008). A previous example of such a system can be seen in the case of HD 80606b (Naef et al. 2001), where the secondary eclipse of the 0.93 eccentricity planet was detected by Laughlin et al. (2009) and later confirmed to also exhibit a primary transit

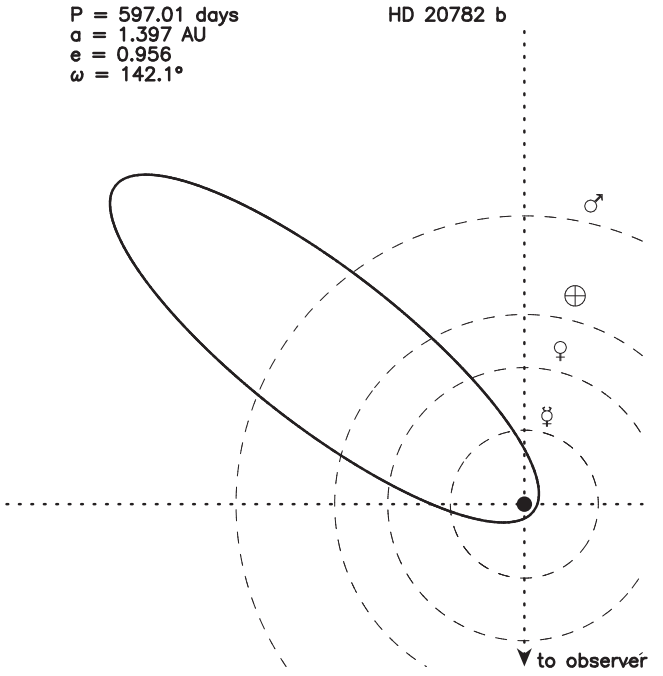

Figure 1. Top-down view of the HD 20782 system based on data described in this paper. The Keplerian orbit of the planet, shown as a solid line, is depicted using the new parameters from Table 4. The orbits of the solar system planets (dashed lines) are shown for comparison.

(Fossey et al. 2009; Garcia-Melendo & McCullough 2009; Moutou et al. 2009). An additional motivation for obtaining high-precision photometry during the transit window and periastron passage for HD 20782b is the possibility of detecting reflected light from the planet since the small star–planet separation will greatly increase the amplitude of the phase signature (Kane & Gelino 2010). Such a detection would allow an estimate of the geometric albedo of the planet and place constraints upon the atmospheric properties and the atmosphere's radiative and advective timescales (Seager et al. 2005; Fortney et al. 2008). Note that since the orbital period is 18 months, an observing opportunity for a particular point in the orbit will only arise every three years since the star will be largely inaccessible to ground-based observers for each alternate orbit.

3. STELLAR PROPERTIES

A critical step in quantifying the properties of the planet lies in understanding the host star. Here we provide new fundamental parameters and abundances for HD 20782.

3.1. Fundamental Parameters

We acquired a high signal-to-noise ratio (300 s integration) spectrum of HD 20782 on the night of 2014 July 6. The data were acquired using CHIRON, a fiber-fed Echelle spectrometer (Tokovinin et al. 2013; Brewer et al. 2014), installed at the 1.5 m telescope at Cerro Tololo Inter-American Observatory. CHIRON operates at a fixed wavelength range of 415–880 nm and a resolution of $R = 79{,}000$. The spectrum was modeled using the Spectroscopy Made Easy (SME) package, described in more detail by Valenti & Piskunov (1996), Valenti & Fischer (2005). SME uses an iterative technique that combines model atmosphere analysis with Yonsei-Yale model isochrones

Table 1
Stellar Parameters

Parameter	Value
V	7.4
$B - V$	0.63
Distance (pc)	35.5 ± 0.8
$T_{\rm eff}$ (K)	5798 ± 44
$\log g$	4.36 ± 0.06
$v \sin i$ (km s^{-1})	1.7 ± 0.5
[Fe/H] (dex)	0.01 ± 0.03
$M_\star$ ($M_\odot$)	1.02 ± 0.02
$R_\star$ ($R_\odot$)	1.09 ± 0.04
Age (Gyr)	5.53 ± 1.43

(Demarque et al. 2004) that utilize *Hipparcos* photometry and distances (van Leeuwen 2007a, 2007b). This approach produces a self-consistent convergence with the measured surface gravity (Valenti et al. 2009).

The results of this analysis are shown in Table 1, including values for the surface gravity $\log g$, rotational velocity $v \sin i$, atmospheric abundance [Fe/H], effective temperature $T_{\rm eff}$ and stellar isochrone solution (mass $M_\star$, radius $R_\star$, and age). These parameters are consistent with previous estimates of the stellar properties, such as those calculated by Takeda et al. (2007). The revised parameters demonstrate that HD 20782 is quite similar to the Sun, with the mass and radius being crucial properties for the subsequent analysis of the planetary companion in this paper.

3.2. Abundances

Both components of the wide binary system, namely HD 20781 and HD 20782, have had their elemental abundances measured by a number of different authors. However, due to the difference in size and spectral type, the abundances within HD 20782 are easier to determine. While half as many groups have measured HD 20781 than HD 20782, there does remain some overlap by some, such as Neves et al. (2009), Delgado Mena et al. (2010), and Mack et al. (2014) who did a more in-depth comparison of the two stars.

Per the analysis in the Hypatia Catalog (Hinkel et al. 2014), the individual abundances within both stars were renormalized to the Lodders et al. (2009) solar scale. The largest measurement discrepancy between data sets, known as the *spread*, was used to better quantify the uniformity, or lack thereof, between measurements. This technique was implemented in the Hypatia Catalog to better understand the variation in abundances seen when employing different reduction techniques, due to instances where the *spread* between groups was larger than associated error. For the cases where variations between groups were small, the median value was used as the ultimate abundance measurement.

The overall median [Fe/H] content in HD 20781 was 0.1 dex, as compared to 0.15 dex within HD 20782, where the spread was 0.03 dex and 0.17 dex, respectively. In other words, the groups that measured HD 20781, while fewer in number, were in closer agreement regarding the iron abundance than those that measured HD 20782. The [Fe/H] determinations for both stars are disparate compared to the abundances determined by Mack et al. (2014), which are not part of the Hypatia Catalog, who measured 0.04 ± 0.03 and -0.02 ± 0.02, respectively. These are consistent with our new [Fe/H] determination shown in Table 1.

A wide variety of α-elements (carbon, magnesium, silicon, and titanium), odd-Z elements (sodium, aluminum, and scandium), and iron-peak elements (vanadium, chromium, cobalt, and nickel) have been measured for both stars. For all elements except for [Na/Fe], the abundance measurements for HD 20781 and HD 20782 were found to be consistent to within error and markedly sub-solar, or ~ -0.1 dex. The [Na/Fe] content in HD 20782 was found to be $\sim$2.5 more than in the companion HD 20781, where [Na/Fe] $= -0.09 \pm 0.06$ dex and -0.22 ± 0.04 dex, respectively.

4. THE KEPLERIAN ORBIT OF THE PLANET

The highly eccentric planet orbiting HD 20782 was first reported in Jones et al. (2006) and updated in O'Toole et al. (2009). We now present a further six years of RV data from the Anglo-Australian Planet Search (AAPS). The AAPS is one of the world's longest-running planet searches, with more than 40 planet discoveries in its 16 years of operation (e.g., Butler et al. 2001; Jones et al. 2010; Vogt et al. 2010; Tinney et al. 2011; Wittenmyer 2012, 2014). HD 20782 has been observed on 52 epochs from 1998 August 9 to 2013 September 19 (Table 2). Precision Doppler measurements are obtained with the UCLES echelle spectrograph (Diego et al. 1990) at the 3.9 m Anglo-Australian Telescope (AAT). A 1 arcsec slit delivers a resolving power of $R \sim 45{,}000$. Calibration of the spectrograph point-spread function is achieved using an iodine absorption cell temperature-controlled at 60.0 ± 0.1°C. The iodine cell superimposes a forest of narrow absorption lines from 5000 to 6200 Å, allowing simultaneous calibration of instrumental drifts as well as a precise wavelength reference (Valenti et al. 1995; Butler et al. 1996). The result is a precise RV shift measured relative to the epoch of the iodine-free "template" spectrum. AAT velocities for HD 20782 span a total of 15 years and have a mean internal uncertainty of 2.4 m s^{-1}.

Orbital fits to the AAT data allowed predictions of the next periastron passage of the planet, estimated to be 2015 January 15. We were able to observe HD 20782 during that passage using the Physical Research Laboratory optical fiber-fed high-resolution cross-dispersed echelle spectrograph (PARAS) with the Mount Abu 1.2 m telescope in India. The PARAS spectrograph is temperature-controlled at 25.55 ± 0.01°C in an enclosure that is pressure-controlled at 0.10 ± 0.03 mbar. PARAS has a resolution of $R \sim 67{,}000$ and obtains RV data at a spectral range of 3800–6900 Å with simultaneous wavelength calibration with a thorium-argon (ThAr) hollow cathode lamp. The uncertainties for the PARAS measurements were derived based on the photon noise estimation procedure explained by Bouchy et al. (2001). Further details of the PARAS instrument and the data reduction are described by Chakraborty et al. (2014). PARAS observations were made under high air mass conditions (1.7–1.9) with no Atmospheric Dispersion Corrector. The five PARAS observations (see Table 3) complete our RV data set and bring the total number of observations to 57.

The RV data shown in Tables 2 and 3 were used to produce a revised Keplerian orbital solution. This was performed using the RVLIN package; a partially linearized, least-squares fitting procedure (Wright & Howard 2009). The uncertainties for the orbital and associated physical parameters were estimated using the BOOTTRAN bootstrapping routines described in

Table 2
HD 20782 AAT Radial Velocities

Date (BJD–2440000)	RV ($m\,s^{-1}$)	σ ($m\,s^{-1}$)
11035.31946	21.90	2.33
11236.93065	−6.51	3.27
11527.01731	7.32	3.39
11630.88241	29.70	2.72
11768.30885	−6.64	2.62
11828.11066	−7.64	3.00
11829.27449	−6.64	3.82
11856.13530	−10.37	3.55
11919.00660	−3.62	2.92
11919.99630	−1.67	2.85
11983.89009	4.16	3.32
12092.30437	17.84	2.35
12127.26814	17.70	2.79
12152.16308	23.15	2.50
12187.15965	22.78	2.53
12511.20636	−1.26	2.29
12592.04809	17.40	2.30
12654.96031	15.38	2.34
12859.30551	−202.48	1.90
12946.13833	−18.15	2.08
12947.12246	−14.27	1.77
13004.00143	−0.29	1.85
13044.02367	0.76	2.25
13045.96088	−0.40	1.93
13217.28800	9.01	1.71
13282.22023	20.57	1.87
13398.96924	22.14	1.39
13403.96059	30.40	2.56
13576.30688	−9.14	1.60
13632.28114	−7.62	1.59
13665.18659	6.38	1.72
14013.21622	31.23	1.55
14040.13171	22.12	1.96
14153.97010	−11.56	2.10
14375.24693	13.32	1.70
14544.89158	10.26	2.15
14776.10092	−7.55	1.85
14843.02077	0.09	1.56
14899.92440	−0.65	2.07
15107.24701	16.54	2.78
15170.05453	17.31	2.37
15204.97966	29.22	1.88
15253.91188	−78.17	2.35
15399.32249	−8.19	1.88
15426.31459	−6.89	1.71
15461.23900	−14.81	2.99
15519.13309	8.36	2.00
15844.13584	−145.90	6.54
15845.17956	−185.60	2.28
15846.13671	−156.28	2.32
15964.93095	7.77	2.87
16499.33740	−11.25	3.03

Table 3
HD 20782 PARAS Radial Velocities

Date (BJD–2440000)	RV ($m\,s^{-1}$)	σ ($m\,s^{-1}$)
57036.16183	272.25	4.12
57038.14436	127.25	4.09
57039.13336	61.53	3.65
57040.15494	149.14	3.86
57042.12356	183.06	2.98

Wang et al. (2012). To be sure that known instabilities of the Levenberg–Marquardt-based RVLIN algorithm did not prevent convergence at these high eccentricities, we reduced the number of nonlinear parameters in the problem by fixing the eccentricity at 100 values evenly spaced between 0.93 and 0.995 and selecting the value that produced the minimum χ^2 fit.

A fit to the AAT and PARAS data with their instrumental uncertainties was unsatisfactory. The rms residuals to the PARAS data are $17\,m\,s^{-1}$, with two excursions at and after RV minimum of over $20\,m\,s^{-1}$, inconsistent with typical instrumental uncertainties of under $6\,m\,s^{-1}$. Further, the scatter about the fit to the AAT data is $6.1\,m\,s^{-1}$, including three excursions larger than $15\,m\,s^{-1}$ (up to $17\,m\,s^{-1}$), both significantly larger than the quoted errors of $2.3\,m\,s^{-1}$. Given that there are only 52 AAT points, we do not expect to see 3 points (∼5%) with deviations of $15\,m\,s^{-1}$ from Gaussian noise unless the errors are more like $6\,m\,s^{-1}$.

Some component of the scatter about the best fit is due to intrinsic stellar variability, and some is due to the precision of the measurements (due to both instrumental/algorithmic imprecision and photon noise). The stellar noise should be the same for both instruments, meaning that the large excursions seen in the PARAS data indicate a problem with either the fit or the PARAS data.

Close examination of points near periastron reveal that the problem must lie with the instrumental uncertainties, not the fit. PARAS and AAT have two measurements (each) at very similar phases (the expected change in RV between the points in each pair is $<10\,m\,s^{-1}$). However, in both cases the difference in velocities is over $20\,m\,s^{-1}$, and in different directions. The combined measurement uncertainties of the two instruments therefore must be of order $20\,m\,s^{-1}$.

We attempted a second fit, but inflated both instrumental uncertainties by adding, in quadrature, 5 and $19\,m\,s^{-1}$ to the AAT and PARAS velocities, respectively. These inflations reflect a common stellar jitter component (likely to be around $5\,m\,s^{-1}$) and an additional, instrument-dependent component added in quadrature. This resulted in a much more satisfactory fit: the residuals to the best fit for the two telescopes have standard deviations of $5.75\,m\,s^{-1}$ and $19.85\,m\,s^{-1}$, respectively, and χ^2 values of 1.03 and 1.01, respectively. There is still a significant outlier to the AAT fit (at $15\,m\,s^{-1}$), but at 2.5σ (using the inflated measurement uncertainties) this is not unexpected from 52 data points.

We conclude that there is significant instrumental/observational systematic noise in the PARAS data due to air mass, of order $20\,m\,s^{-1}$. We also examined the inclusion of a linear RV trend in our model but found that this does not improve the quality of the fit. The final orbital solution from the data is shown in Table 4, where we have included the solution that uses the AAT data only for comparison. The AAT+PARAS orbital solution includes an offset between the AAT and PARAS data sets as a free parameter, found to be $276.5 \pm 8.7\,m\,s^{-1}$. The γ parameter shown in Table 4 is the systemic velocity of the system with respect to the zero point of the extracted RVs (relative to the template spectrum). Thus, there is an offset between the γ value reported in Table 4 and the true systemic velocity, reported by Valenti & Fischer (2005) to be $40.7\,km\,s^{-1}$. Our final AAT+PARAS orbital

Table 4
Keplerian Orbital Model

Parameter	Value (AAT)	Value (AAT+PARAS)
HD 20782 b		
P (days)	597.099 ± 0.049	597.065 ± 0.043
T_c[a] (BJD–2,440,000)	17037.788 ± 0.145	17037.794 ± 0.100
T_p[b] (BJD–2,440,000)	17038.510 ± 0.108	17038.458 ± 0.094
e	0.953 ± 0.005	0.956 ± 0.004
ω (deg)	142.2 ± 2.2	142.1 ± 2.1
K (m s^{-1})	114.9 ± 4.4	116.0 ± 4.2
$M_p \sin i$ (M_J)	1.46 ± 0.03	1.43 ± 0.03
a (au)	1.397 ± 0.009	1.397 ± 0.009
System properties		
γ (m s^{-1})	1.95 ± 0.82	1.79 ± 0.80
Measurements and model		
N_{obs}	52	57
rms (m s^{-1})	5.91	8.06
χ^2_{red}	1.0	1.14

Notes.
[a] Time of mid-transit.
[b] Time of periastron passage.

solution is depicted in Figure 2. The bottom panel of Figure 2 shows the quality of the combined data coverage during periastron passage for this highly eccentric planet, particularly the additional coverage provided by the PARAS data.

We note that the transit time we calculate is sensitive to the weights assigned to the PARAS and AAT data. The PARAS data favor a transit time that is 0.2–0.3 days later than the AAT data. Because we do not fully understand the source of the very large scatter in the PARAS data, we should not assume that our errors are Gaussian. Fortunately, BOOTTRAN uses bootstrapping to determine its parameter uncertainties, which is appropriate for non-normally distributed residuals (although the underlying fitter minimizes χ^2, and so does assume Gaussian errors).

5. ASTROMETRIC CONSTRAINTS ON THE ORBIT

To constrain the inclination of the system and possibly refine the estimate of the companion mass, we combine *Hipparcos* astrometry of HD 20782 with the orbital parameters obtained from the RV observations. We use the new reduction of the *Hipparcos* data (van Leeuwen 2007a), which presents a significant improvement in the overall reliability of astrometric information (van Leeuwen 2007b) and includes the Intermediate Astrometric Data (IAD) product in a format that facilitates the quest for signatures of orbital motion. Following the method prescribed by Sahlmann et al. (2011), we use the spectroscopic elements derived from our RV solution (Table 4) to search for an orbital signature.

The five standard astrometric parameters for the *Hipparcos* solution of a HD 20782 can be obtained from the VizieR Catalog (van Leeuwen 2007a); these are right ascension (R.A., $\alpha = 50.^\circ01$), declination (decl., $\delta = -28.^\circ85$), proper motion in R.A. ($\mu_\alpha = 349.33$ mas yr^{-1}) and decl. ($\mu_\delta = -65.92$ mas yr^{-1}), and parallax ($\varpi = 28.15$ mas). The 5 spectroscopic parameters required from the RV analysis are period (P), eccentricity (e), semi-amplitude (K), time of periastron (T_0), and argument of periastron (ω). Each *Hipparcos* observation is reconstructed from the IAD and fit with a comprehensive model based on 12 parameters: the five standard astrometric parameters, the five

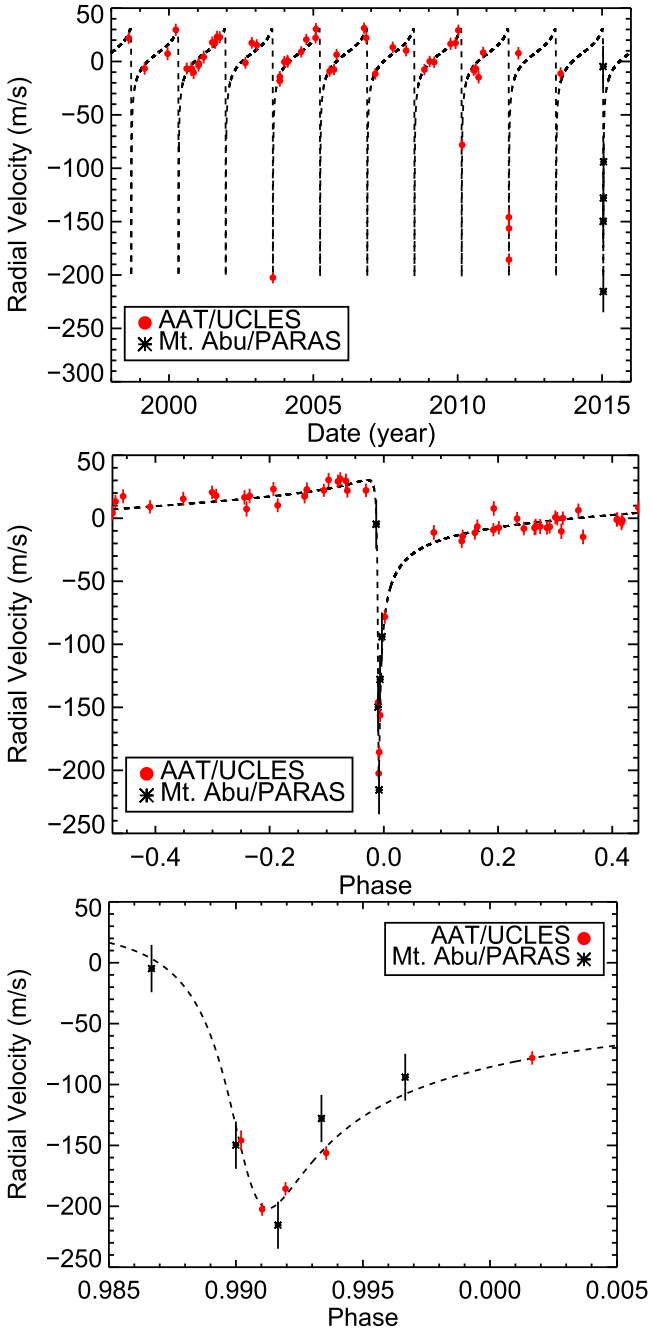

Figure 2. Top: all 57 RV measurements from AAT/PARAS observations of HD 20782 (see Tables 2 and 3) along with the best-fit orbital solution (Table 4). RV offsets between data sets have been accounted for in this figure. Middle: the RV data phased on the orbital the solution from Table 4, where phase zero corresponds to superior conjunction. Bottom: a zoomed version of the phased middle plot which shows the coverage during periastron passage.

spectroscopically derived parameters, the inclination (i), and the longitude of the ascending node (Ω). In practice, the spectroscopic parameters are treated as constants since they are considered reliable, and we work with seven free parameters. The details of the procedure are carefully described by Sahlmann et al. (2011), and we follow their methods to calculate inclination, a new orbit, and the significance of the orbit via the permutation test.

We begin by constructing a two-dimensional $i - \Omega$ grid, where we solve for the remaining five parameters of the

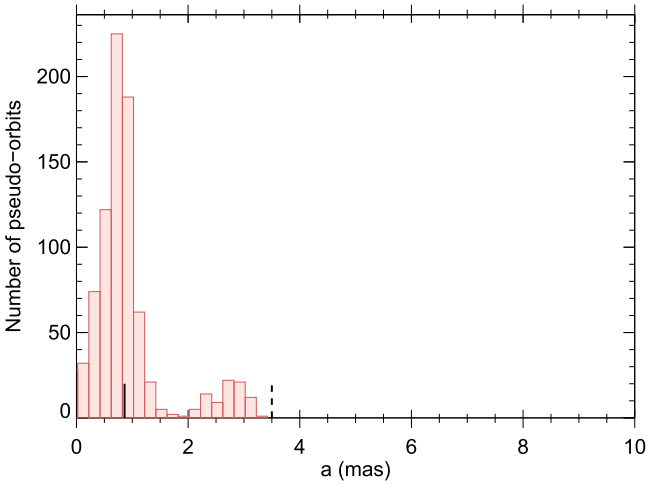

Figure 3. Histogram of the semimajor axes for 1000 randomly permuted pseudo-orbits of HD 20782. The pseudo-orbits are used to calculate the significance of the new orbit via the permutation test, as described by Sahlmann et al. (2011). The solid black line shows the actual best-fit solution and the dashed line represents the median *Hipparcos* single-measurement precision for this system.

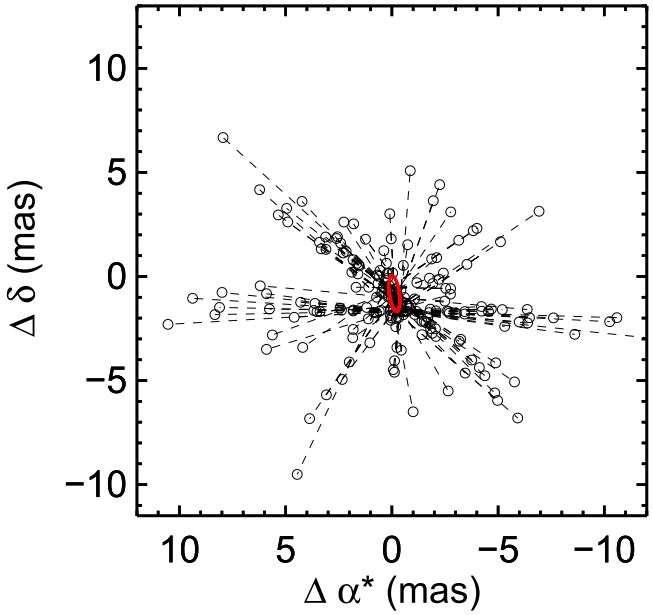

Figure 4. Red line shows the orbital signature detected in the *Hipparcos* data when combined with orbital parameters from the radial velocity solution. As projected on sky, north is up and east is left. Open circles mark the individual *Hipparcos* measurements. Dashed lines with orientation along the scan angle ψ and length given by the residual of the orbital solution connect the measurements with the predicted location from our model. This illustrates the difficulty of detecting an orbit with such a small projected semimajor axis, given the median *Hipparcos* single-measurement precision on this target.

seven-parameter model, and the corresponding χ^2. The parameter values identified by the minimum χ^2 value are used as the starting point for an *AMOEBA* minimization, using the downhill simplex method, to supersede the limitations imposed by the resolution of the $i - \Omega$ grid. We then perform 100,000 Monte Carlo simulations, where we generate 1000 sets of *Hipparcos* measurements from the existing data. For each set of *Hipparcos* abscissae, we execute 100 random draws from the spectroscopic parameters, in order to inculcate their uncertainties into our result. Each spectroscopic parameter is assumed to be a Gaussian distribution, with the RV solution and its errors serving as the mean and standard deviation respectively. The Monte Carlo models are then solved as described above, to produce 100,000 sets of solution parameters. The final parameters are defined as the median of the associated distribution, while the errors are the interval between the 15.85 percentile and the 84.15 percentile, encompassing 68.3% of the values around the median.

For completeness, we report here our full set of final parameters, as offsets to the *Hipparcos* values. The changes in R.A., decl., parallax, proper motion in R.A. and decl., and the argument of periastron are $\Delta\alpha = 0.3^{+1.4}_{-1.2}$ mas, $\Delta\delta = 1.0^{+1.3}_{-1.1}$ mas, $\Delta\varpi = 0.2^{+0.7}_{-0.7}$ mas, $\Delta\mu_{\alpha^\star} = 0.0^{+0.4}_{-0.4}$ mas yr^{-1}, $\Delta\mu_\delta = 0.1^{+0.6}_{-0.6}$ mas yr^{-1}. We find an inclination of $2\overset{\circ}{.}7^{+2.3}_{-1.2}$ and an argument of periastron $202\overset{\circ}{.}5^{+59.3}_{-66.3}$, but the solution is very poorly constrained.

The astrometric data covers approximately two orbits for this system, so phase coverage should not inhibit the recovery of any significant orbital signatures. Unfortunately, the projected minimum semimajor axis of our new solution is very small ($a \sin i = 0.05$ mas) compared to the median *Hipparcos* single-measurement precision for this target (3.5 mas), as shown in Figures 3 and 4. We perform a permutation test to verify the significance of our result by comparing the semimajor axis of the new solution orbit with 1000 pseudo orbits generated from random permutations of the astrometric data, similar to Sahlmann et al. (2011). Figure 3 illustrates the calculation of a low significance orbit (68.2%, which is almost exactly at the 1σ level of detection), confirming that the *Hipparcos* data contains little or no orbital signature. The new *Hipparcos* reduction has this target flagged as having a good fit with just the five astrometric parameters, which is consistent with the fact that adding the seven RV parameters does not seem to change the solution. Sahlmann et al. (2011) emphasize that orbital solutions at this significance level are prone to very large biases, and the calculated values and their errors should be considered highly suspect. We present our full set of orbital parameters here only to facilitate future comparison of analytical methods, and not for direct application.

On the other hand, simulations by Sahlmann et al. (2011) show that orbits are always detected at the 3σ level when the semimajor axis is at least 70% of the *Hipparcos* precision on a target. Any orbital signature above 2.45 mas would have been detectable in this *Hipparcos* data set, and this helps to set an upper limit on the companion mass. Using this assertion, we get a lower limit on inclination ($1\overset{\circ}{.}22$) and an upper limit on the companion mass ($66\,M_J$). Although the consideration of astrometric data does not allow us to put tight constraints on the inclination of the system, the non-detection of an orbit allows us to rule out a stellar binary system. Verification of this could be achieved through high-contrast adaptive-optics imaging of the system at predicted apastron passage. Figure 5 shows the projected and angular separation of the planet and star for one complete face-on orbit, where phase zero corresponds to superior conjuction as described by Kane (2013). An additional consequence of our astrometric constraint is that the transit probability is increased by a small amount since inclinations below $1\overset{\circ}{.}22$ are ruled out.

6. PLANETARY TRANSIT PROSPECTS

As described in Section 2, one of the most interesting aspects of HD 20782b is the relatively large transit probability

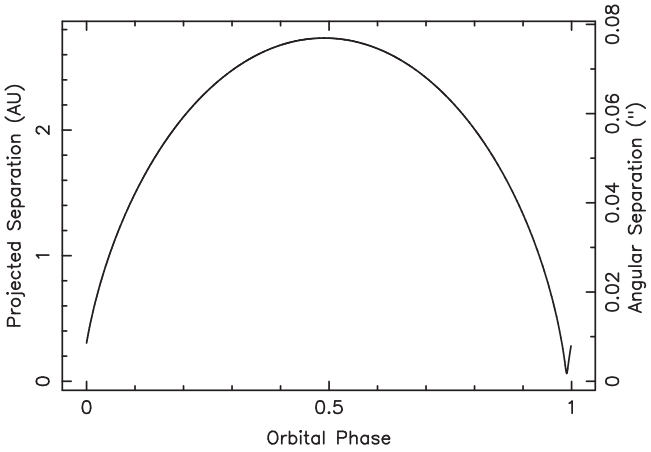

Figure 5. Projected (au) and angular (″) separation of HD 20782b from the host star as a function of orbital phase, where phase zero corresponds to superior conjunction.

compared with the orbital period. The transit probability is a function of the stellar and planetary radii and the star–planet separation along the line of sight (Kane & von Braun 2008). For HD 20782, we use the stellar radius shown in Table 1 and adopt a planetary radius of $R_p = 1.0\ R_J$ given the minimum mass of 1.41 M_J (see Table 4) and using the mass–radius relationship described by Kane & Gelino (2012a).

If the planet were in a circular orbit with the same semimajor axis, the transit probability would be 0.4%. The extreme eccentricity of the orbit results in star–planet separation of 0.061 au at periastron and 0.076 au at inferior conjunction where a transit is possible. Such a separation is similar to that of a hot Jupiter in a circular orbit. Inferior conjunction occurs when $\omega + f = 90°$; in this case, the true anomaly is $f = 307.°9$ at the time of mid-transit. This orbital orientation results in an enhanced transit probability of 7.1%.

A further influence of the high eccentricity on the transit parameters is the expected transit duration. Since the separation at inferior conjunction is comparable to a hot Jupiter, the duration is likewise reduced and has an amplitude of 0.13 days (3.1 hr) for a central transit. The epoch of mid-transit shown in Table 4 was calculated using the same Monte-Carlo bootstrap method used to calculate the orbital parameter uncertainties. The time of mid-transit corresponds to a calendar date of 2015 January 15 and a UT of 7:02. The uncertainty on this time is 0.1 days which results in a total 1σ transit window of 0.33 days (7.6 hr). The estimated depth of the transit is 0.96% and so should be readily observable in typical millimag photometry. However, the infrequent occurrence of such events (see Section 2) motivated observations from both ground and space.

7. PHOTOMETRIC OBSERVATIONS

The derived physical and orbital properties of HD 20782b described in previous sections motivated photometric monitoring of the host star for stellar variability and planetary transit/phase signatures. Here we describe our photometric observations and results in detail.

7.1. APT Photometry

We collected a total of 191 nightly photometric observations of HD 20782 during its 2013–14, 2014–15, and 2015–16 observing seasons to search for stellar variability. The observations were acquired with the T8 0.80 m automatic photoelectric telescope (APT), one of several automated telescopes operated by Tennessee State University (TSU) located at Fairborn Observatory in southern Arizona. The T8 APT is equipped with a two-channel precision photometer that uses a dichroic filter and two EMI 9124QB bi-alkali photomultiplier tubes to measure the Strömgren b and y passbands simultaneously. We computed the differential magnitudes of HD 20782 with respect to the mean brightness of its three constant comparison stars. To improve the precision further, we combined the differential b and y observations into a single $(b + y)/2$ "passband." The TSU APTs, their precision photometers, observing strategy, and data reduction techniques are described in detail by Henry (1999). A summary of the photometric data for HD 20782 is given in Table 5.

Table 5
Summary of Photometric Observations for HD 20782

Observing Season	N_{obs}	Julian Date Range (HJD–2,400,000)	Mean (mag)	Sigma (mag)
2013–14	43	56622–56701	1.01241	0.00183
2014–15	89	56943–57045	1.01206	0.00228
2015–16	59	57293–57390	1.01128	0.00171

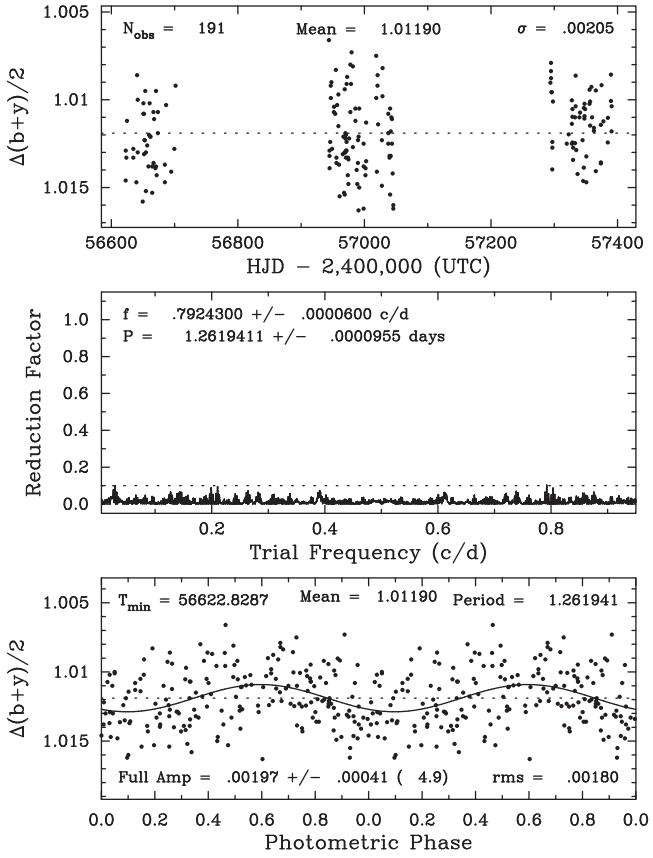

Figure 6. HD 20782 APT photometry acquired during three consecutive observing seasons. Top: the relative photmetry as a function of Heliocentric Julian Date. Middle: the power spectra from a Fourier analysis of all seasons photometry. Bottom: sinusoidal fit to the most significant period found from the Fourier analysis. Our analysis described in the text demonstrates that this period is spurious.

The nightly observations of HD 20782 are plotted in the top panel of Figure 6 in our $(b + y)/2$ passband. The observing

seasons are quite short from Fairborn Observatory, only three months in length, because of the star's southerly declination of −29°. The observations scatter about their grand mean (indicated by the horizontal dotted line) with a standard deviation of 0.00205 mag, as given in the upper right corner of the top panel. This is essentially the limit of precision for the HD 20782 observations because the star's southerly declination results in all measurements being made at air mass values between 2.0 and 2.4 (see Henry 1999, Figure 8).

The middle and bottom panels of Figure 6 show the frequency spectrum of the data set and the phase curve computed with the best frequency, respectively. Our frequency analysis is based on least-squares sine fits with trial frequencies between 0.01 and 0.95 c/d, corresponding to periods between one and 100 days. The goodness of fit at each frequency is measured as the reduction factor in the variance of the original data, whose value lies between the extremes of 0.0 and 1.0. A reduction factor of 0.0 corresponds to the case where the variance in the residuals from a least-squares sine fit to the observational data at some trial frequency have the same value as the variance in the original data, i.e., no reduction in the variance takes place at that particular frequency. A reduction factor of 1.0 corresponds to the extreme case where the variance in the residuals of the sine fit is 0.0, i.e., the sine curve fits the data perfectly with no residuals. The frequency spectrum in the middle panel shows several peaks with reduction factors near 0.1, but no peak stands out above the others to suggest a stellar rotation period. We ran simulations adding computed sine curves to our data sets and found that coherent variations with peak-to-peak amplitudes of ∼0.004 mag or larger would be detectable in our light curves. This places an upper limit to any periodic modulation for HD 20782, such as rotational modulation caused by starspots. This is consistent with the low level of magnetic activity ($\log R'_{HK} = -4.91$) given in the discovery paper of Jones et al. (2006) and demonstrates that our best-fit period of 1.2619 days in the bottom panel is spurious. In addition to the absense of rotational modulation, we find no evidence for longer-term variability; the three seasonal means in Table 5 scatter about their grand mean with a standard deviation of only 0.00058 mag.

7.2. MOST Observations and Transit Window

Given the size of the transit windows and the relatively infrequent opportunities to observe them (see Sections 2 and 6), we elected to make use of the *MOST* satellite to observe HD 20782 during the next scheduled transit window. *MOST* has an aperture of 15 cm and a filter passband covering the range 375–675 nm, making it well-suited to obtain precision optical photometry of very bright stars (Walker et al. 2003; Matthews et al. 2004).

Observations of HD 20782 commenced at HJD 2457035.3 (2015 January 12 19:11 UT) and concluded seven days later at HJD 2457042.3 (2015 January 19 19:11 UT). The predicted time of mid-transit (see Table 4) was BJD 2457037.794 (2015 January 15 07:02 UT). The star is outside of *MOST*'s Continuous Viewing Zone and so required observations outside of normal operational parameters. For each 101 minutes orbit, *MOST* was able to acquire the target field for 20 minutes. Exposure times were 0.6 s to allow for both the brightness of the target and scattered light due to the roll angle of the spacecraft with respect to the Sun. This resulted in photometry with a 1σ rms precision of 0.07%.

During the week of *MOST* observations, a total of 257 measurements of HD 20782 were acquired. The resulting relative photometry of the data are shown in Figure 7, along with a solid line that indicates the predicted location and depth of a possible transit. The 1σ transit window (0.33 days) was described in Section 6. We use the 3σ transit window (0.43 days) to draw vertical dashed lines in Figure 7. A central transit of the planet (impact parameter of $b = 0$) is ruled out for most locations within the transit window. The cadence of the observations is such that a transit duration half that of a central transit could have been missed within the 1σ transit window. Such a duration corresponds to an impact parameter of $b = 0.87$, above which transits cannot be ruled out by our photometry.

A further consideration is the detection of the Rossiter–McLaughlin (R–M) effect during a possible transit. The amplitude of the R–M effect is shown by (Gaudi & Winn 2007) to be

$$K_R = v \sin i \frac{(R_p/R_\star)^2}{1 - (R_p/R_\star)^2}. \quad (1)$$

Using our stellar parameters from Table 1 and the transit parameters described in Section 6, the amplitude of the R–M effect for a transit of HD 20782b is predicted to be ∼15.5 m s^{-1}. Two of our RV measurements (one each from AAT and PARAS) are within the transit window, shown close to 0.5 phase in the bottom panel of Figure 2. Neither of these measurements show evidence of any significant deviation from our Keplerian model. Thus, the RV data are consistent with the *MOST* photometry leading to the conclusion that the planet does not transit the host star.

7.3. Evidence of Phase Variations

The phase variations of a planet as it orbits the host star has become a detectable signature in the era of high-precision photometry. Numerous examples of phase signatures have been detected from the planets detected with the *Kepler* mission (Esteves et al. 2013, 2015).

Exoplanets that are close to their host stars have generally been found to have low geometric albedos, such as the low geometric albedo of HAT-P-7b (Welsh et al. 2010) and the null detection of phase variations from HD 209458b (Rowe et al. 2008). There are exceptions to the rule, however, such as the case of Kepler-7b (Demory et al. 2011), and it is likely that a greater understanding of atmospheric processes is needed to explain this diversity (Demory 2014). Kane & Gelino (2010) developed a geometric albedo model that scales the geometric albedo with star–planet separation. The implication of the model for planets in eccentric orbits is that the geometric albedo is time dependent, with an assumption that reflective/scattering condensates in the upper atmosphere are removed during periastron passage by the increase in radiative flux from the host star. The generalized expression for the planet to host flux ratio is given by

$$\epsilon(\alpha, \lambda) \equiv \frac{f_p(\alpha, \lambda)}{f_\star(\lambda)} = A_g(\lambda) g(\alpha, \lambda) \frac{R_p^2}{r^2} \quad (2)$$

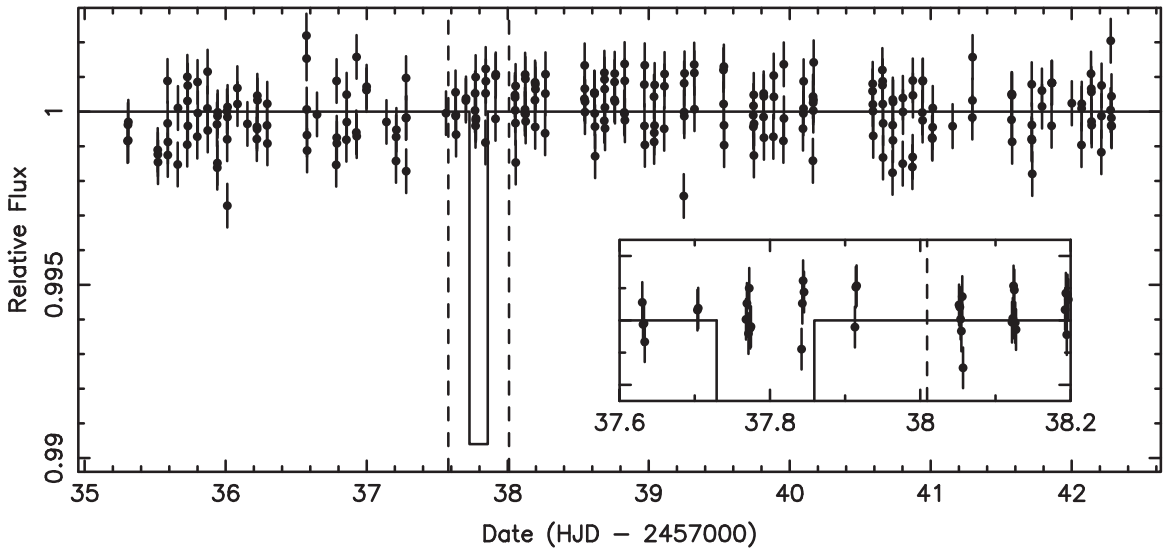

Figure 7. *MOST* photometry of HD 20782 acquired for ~7 days surrounding the predicted transit mid-point. The solid line indicates the location and depth of a possible transit and the vertical dashed lines are the boundaries of the 3σ transit window.

where α is the phase angle, A_g is the geometric albedo, g is the phase function, R_p is the planetary radius, and r is the star–planet separation. This separation is given by

$$r = \frac{a(1 - e^2)}{1 + e\cos f} \quad (3)$$

where f is the true anomaly. The phase angle, α, is defined to be zero at superior conjunction. A model of geometric albedo time-dependence assumes that the planetary atmosphere responds to the change in incident flux on timescales comparable to the duration of the periastron encounter. This effect has been modeled for the eccentric planet HAT-P-2b at infrared wavelengths by Lewis et al. (2013). Thus Kane & Gelino (2010) predicted that, although the largest phase variations of eccentric planets occur during a relatively short fraction of their orbital phase, the amplitude of the signature would be lowered by the subsequent darkening of their atmospheres during periastron.

For HD 20782b, we calculated the predicted phase variations of the planet with respect to the inferior conjunction (transit) and periastron times, shown as a dashed line in the top panel of Figure 8. These orbital locations are very close to each other (see Figure 1), separated by only 0.66 days. The location of superior conjunction where $\alpha = 0$ occurs 5.63 days after the periastron passage. All three of these orbital locations are covered by the *MOST* observations described in Section 7.2. We include the additional effects of ellipsoidal variations (Drake 2003; Zucker et al. 2007; Kane & Gelino 2012b) and Doppler boosting (Loeb & Gaudi 2003; Faigler & Mazeh 2011) in the top panel of Figure 8, shown as dotted and dot-dashed lines, respectively. The combined effect of all three (phase variations, ellipsoidal variations, and Doppler boosting) is shown as a solid line. For the ellipsoidal component, we have assumed a gravity darkening exponent of $\beta = 0.32$ (Lucy 1967). For the Doppler boosting coefficient, we calculate a value of $\alpha_{\rm beam} = -1.21$ using the stellar temperature from Table 1 and the methodology of Loeb & Gaudi (2003). Using the model of a distance-dependent geometric albedo and Hilton phase function (Kane & Gelino 2010), we determined that the amplitude of the phase variations is comparable to the Doppler boosting, whereas the ellipsoidal component is a minor contribution to the total flux variations. Another point worth noting is that this model assumes an orbit that is close to edge-on. The effect of orbital inclination on the relative amplitudes of the three contributing components is minor except for orbits close to face-on (Kane & Gelino 2011a).

As described in Section 7.2, the original intent of acquiring the *MOST* data was for the purpose of observing a potential transit event. Evidence of phase variations was unexpected due to the low predicted amplitude shown in the top panel of Figure 8. To determine the overall trend in the *MOST* data, we calculated a running mean of the data using 20 data points either side of each measurement to calculate the running mean at that location. The results of this calculation are shown as a solid line along with the individual measurements (including error bars) in the middle panel of Figure 8, where we have adjusted the vertical scale of the plot to the range of the running mean values, using the average of the running mean values as the zero-point. The apparent brightening of the host star between the truncated dates of 38 and 39 on the plot is where the peak of the phase variations are predicted to occur. This was diagnosed from an instrumentation point of view, and it was determined that the change in the brightness was not caused by any aspect of the *MOST* instrumentation or data reduction issues.

We tested the likelihood whether this could be caused by an alignment between intrinsic stellar variability and the expected periastron passage, by conducting a Monte-Carlo simulation in which we treat the observed data as representative of possible stellar variability and randomly rearrange the data to see how often a similar chance alignment can occur. Each random permutation of the observed flux values to the times of observation resulted in a new data set for which the running mean was calculated and then analyzed for significant peaks in the flux. The percentage of simulations for which a specific criteria was met was taken as the probability that the criteria would have been satisfied by chance. Based on 10,000 realizations of this simulation, the probability of a peak occurring in the 38–39 date range is ~17%, and the probability

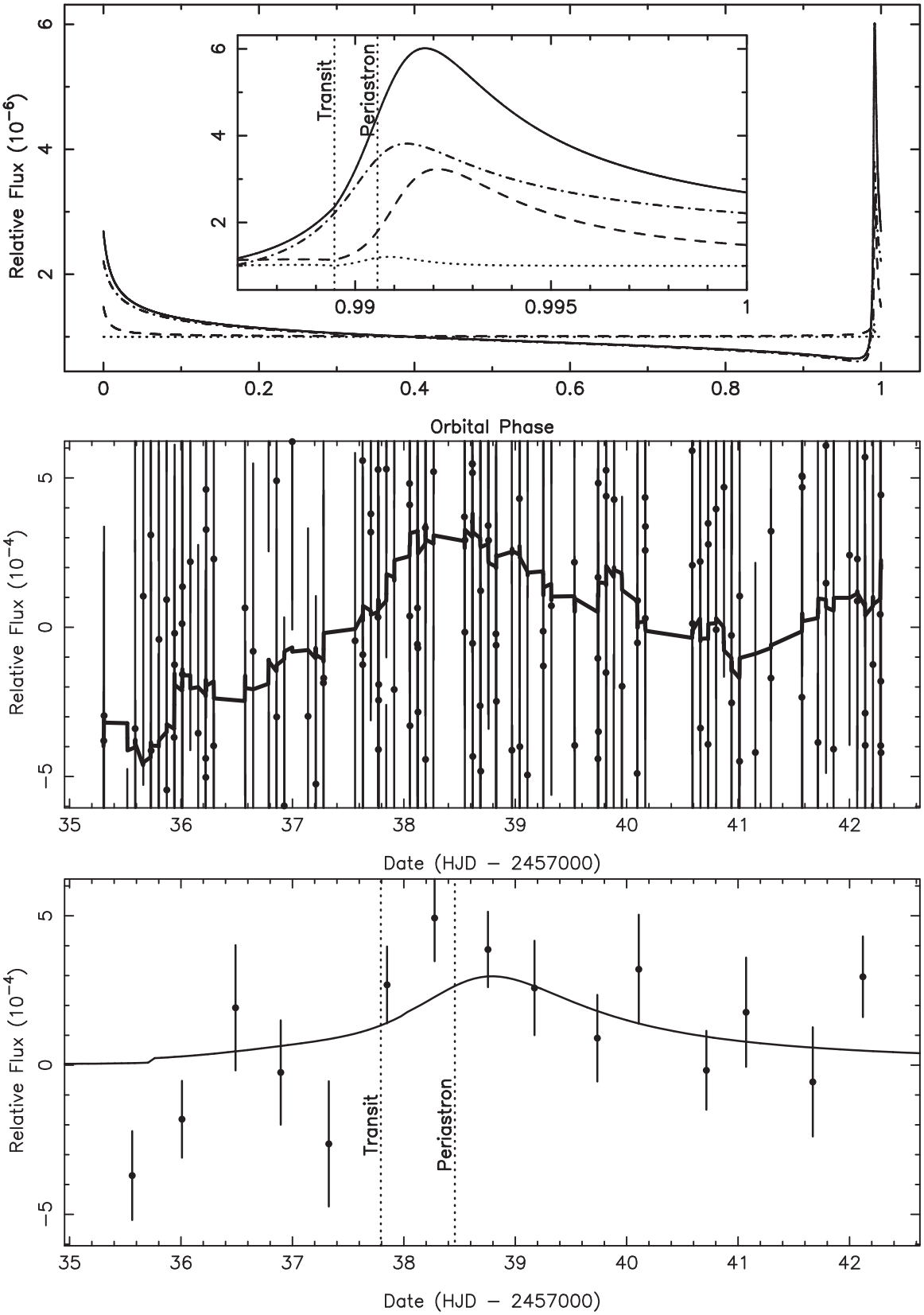

Figure 8. Top: the predicted flux variations of the HD 20782 system due to reflected light from the planet (dashed line), ellipsoidal variations (dotted line), and Doppler boosting (dotted–dashed line). The sum of these three effects is shown as a solid line. This assumes a time-varying geometric albedo, as formulated by Kane & Gelino (2010). The zoomed panel shows the maximum phase variation along with the orbital phase location of periastron and the predicted transit time described in Section 6. Middle: the *MOST* data with the running average shown as a solid line. Bottom: the binned *MOST* data along with a model of the phase variations.

of that peak being of equal or greater amplitude than the observed peak is ∼4%. If indeed the observed peak is related to the close passage of the planet to the star, the flux variations may indicate that the assumption by Kane & Gelino (2010) that the presence of reflective condensates in a planetary atmosphere changes on timescales comparable with the periastron passage is likely incorrect for highly eccentric orbits. In fact, the larger the eccentricity, the more inconsistent the assumption becomes with the radiative and advective timescales of the atmosphere. Furthermore, the possible presence of phase variations indicates the companion is not self-luminous, further supporting the claim that the companion is planetary rather than stellar in nature (Kane & Gelino 2012b).

To investigate this further, we binned the *MOST* photometry into 15 evenly spaced time intervals. The best-fit model to the binned data is shown in the bottom panel of Figure 8 where the model includes ellipsoidal variations and Doppler boosting as well as phase variations. The best-fit inclination of the planetary orbit is $i = 30°$. A fit of the data to both the described model and a constant model resulted in $\Delta\chi^2 = 24$ which shows that the phase model is quantitatively favored. However, the model uses a companion radius of ∼5 Jupiter radii and a geometric albedo of unity, which is a physically unlikely scenario. Thus there is either an additional component missing in our model of the data, or the data may be insufficient to fully characterize the flux variations, or some combination of the two. As noted above, the most compelling aspects of the variations described here are the timing of the variations with those predicted by the phase model, combined with the extreme eccentricity of the planet. This system is clearly highly unusual among the known exoplanets, and we cannot exclude the possibility of unaccounted for physics occuring during the extreme conditions of periastron.

A possible missing factor is that of thermal emission. This has been shown to be a significant component at the *Kepler* passband (Demory et al. 2011). The *Kepler* passband however is significantly broader than that used by *MOST* (see Section 7.2). We calculated this component for our observations by estimating the equilibrium temperature of the planet. To do so, we assumed the most extreme case of zero heat redistribution (hot dayside) and zero Bond albedo (Kane & Gelino 2011b). This produces a peak equilibrium temperature at periastron of ∼1400 K. The resulting blackbody spectrum is shown in Figure 9 along with the passband of *MOST*, depicted as vertical dashed lines. Of the integrated flux from the thermal emission, only 0.02% of the total flux falls within the passband of our observations. This corresponds to a flux ratio of planet to star thermal emission in the *MOST* passband of $\sim 1.5 \times 10^{-6}$. We conclude that any phase variations due to the planet are dominated by the optical component. Further data with higher precision are needed to confirm the presence of the variations and constrain the reflective properties of this fascinating planet as it passes through periastron.

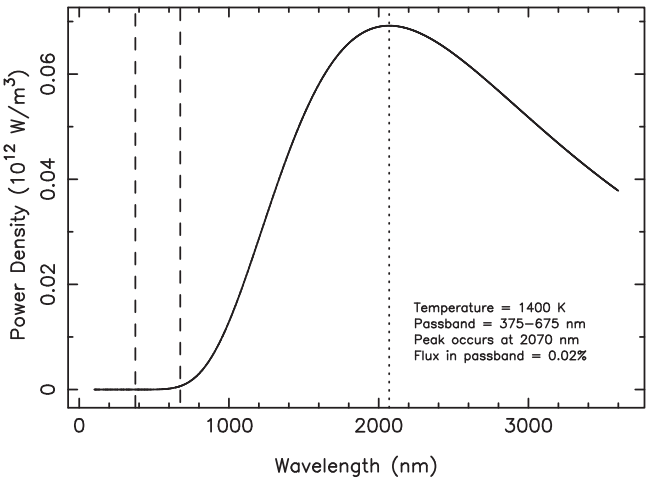

Figure 9. Predicted blackbody flux of HD 20782b, assuming a calculated temperature of ∼1400 K. The passband boundaries of *MOST* are indicated by the vertical dashed lines. The blackbody calculation assumes zero Bond albedo and zero heat redistribution (hot dayside model) and thus represents a maximum flux scenario. Of the integrated flux, 0.02% falls within the *MOST* passband.

8. CONCLUSIONS

Exoplanets in eccentric orbits remain some of the most intriguing discoveries of recent decades. Although the semi-amplitude of their RV variations is systematically higher, the orbits of highly eccentric planets are difficult to characterize due the rapid variation at periastron passage. We have refit the orbit of HD 20782b, consistent with it being the most extreme of these eccentricity cases and have provided new stellar and planetary parameters. Our RV measurements acquired during the brief duration of periastron passage allow a detailed orbital ephemeris to be constructed, despite the relatively long period of ∼18 months. Our analysis of the *Hipparcos* astrometry for HD 20782 constrains the inclination sufficiently such that the companion is likely to be planetary rather than stellar. The uncertainties associated with our astrometric analysis leave open the possibility that the companion lies within the brown dwarf mass regime. It is expected that further astrometric data from the *Gaia* mission will significantly improve these constraints (Perryman et al. 2014). Even with a relatively high transit probability of ∼7%, we have shown that the planet does not transit the host star.

The possible phase variations soon after periastron might be induced in part by stellar light reflected off the planet's atmosphere. Although our modeling is incomplete, if this hypothesis is true then it raises interesting questions regarding the conditions to which such an extreme orbit exposes the planet. In particular, the effects of rotation rate and radiative/advective timescales on atmospheric dynamics may be overwhelmed by the short yet intense conditions that occur at the closest approach of the planet to the star. It has been further noted by several studies that the brightest region of the planet is shifted westward of the substellar point, caused by a relatively cloudy western hemisphere (Demory et al. 2011; Esteves et al. 2015; Hu et al. 2015; Shporer & Hu 2015). Additionally, it seems likely that, although planets in short-period orbits tend to have relatively low geometric albedos, long-period planets in eccentric orbits retain a high geometric albedo during the periastron passage since the atmosphere does not have time to respond to the change in incident flux. The result of this is a higher than expected flux ratio of the planet to the star at optical wavelengths. Thus, eccentric planets present a particularly lucrative observing opportunity for the study of planetary atmospheres, provided one is able to accurately predict when the peak flux variations are expected to occur.

Further observations of this system at times close to inferior conjunction are highly encouraged. The next two times of inferior conjunction predicted from our ephemeris are BJD

2457634.859 ± 0.123 (2016 September 3 8:36 UT) and BJD 2458231.924 ± 0.153 (2018 April 23 10:10 UT). In each case, the subsequent superior conjunction occurs ∼6.29 days after the inferior conjunction. Matching these times to those when the target is most visible is not trivial and the timescale of the periastron passage is best suited to continuous space-based observations. Possibilities for these upcoming windows would be a perfect use for upcoming missions that are optimized for bright star observations, such as the *CHaracterizing ExOPLanet Satellite* (CHEOPS). A deeper understanding of the orbits and atmospheres of eccentric planets are key milestones toward unlocking the origin and nature of these mysterious objects.

The authors thank the anonymous referee, whose comments greatly improved the quality of the paper. S.R.K. and N.R.H. acknowledge financial support from the National Science Foundation through grant AST-1109662. G.W.H. acknowledges long-term support from Tennessee State University and the State of Tennessee through its Centers of Excellence program. H.R.A.J. acknowledges support from STFC via grants ST/M001008/1 and Leverhulme Trust RPG-2014-281. The authors thank the Gurushikar, Mount Abu Observatory staff and the PARAS technical staff for the observations with PARAS. The PARAS program is supported completely by the Physical Research Laboratory, Department of Space, Government of India. The results reported herein benefited from collaborations and/or information exchanged within NASA's Nexus for Exoplanet System Science (NExSS) research coordination network sponsored by NASA's Science Mission Directorate.

REFERENCES

Bouchy, F., Pepe, F., & Queloz, D. 2001, A&A, 374, 733
Brewer, J. M., Giguere, M., & Fischer, D. A. 2014, PASP, 126, 48
Butler, R. P., Marcy, G. W., Williams, E., et al. 1996, PASP, 108, 500
Butler, R. P., Tinney, C. G., Marcy, G. W., et al. 2001, ApJ, 555, 410
Butler, R. P., Wright, J. T., Marcy, G. W., et al. 2006, ApJ, 646, 505
Chakraborty, A., Mahadevan, S., Roy, A., et al. 2014, PASP, 126, 133
Chatterjee, S., Ford, E. B., Matsumura, S., & Rasio, F. A. 2008, ApJ, 686, 580
Delgado Mena, E., Israelian, G., González Hernández, J. I., et al. 2010, ApJ, 725, 2349
Demarque, P., Woo, J.-H., Kim, Y.-C., & Yi, S. K. 2004, ApJS, 155, 667
Demory, B.-O. 2014, ApJL, 789, L20
Demory, B.-O., Seager, S., Madhusudhan, N., et al. 2011, ApJL, 735, L12
Diego, F., Charalambous, A., Fish, A. C., & Walker, D. D. 1990, Proc. Soc. Photo-Opt. Instr. Eng., 1235, 562
Drake, A. J. 2003, ApJ, 589, 1020
Esteves, L. J., De Mooij, E. J. W., & Jayawardhana, R. 2013, ApJ, 772, 51
Esteves, L. J., De Mooij, E. J. W., & Jayawardhana, R. 2015, ApJ, 804, 150
Faigler, S., & Mazeh, T. 2011, MNRAS, 415, 3921
Fortney, J. J., Lodders, K., Marley, M. S., & Freedman, R. S. 2008, ApJ, 678, 1419
Fossey, S. J., Waldman, I. P., & Kipping, D. M. 2009, MNRAS, 396, L16
Garcia-Melendo, E., & McCullough, P. R. 2009, ApJ, 698, 558
Gaudi, B. S., & Winn, J. N. 2007, ApJ, 655, 550
Goldreich, P., & Soter, S. 1966, Icar, 5, 375
Henry, G. W. 1999, PASP, 111, 845
Hinkel, N. R., Timmes, F. X., Young, P. A., Pagano, M. D., & Turnbull, M. C. 2014, AJ, 148, 54
Hu, R., Demory, B.-O., Seager, S., Lewis, N., & Showman, A. P. 2015, ApJ, 802, 51
Jones, H. R. A., Bulter, R. P., Tinney, C. G., et al. 2010, MNRAS, 403, 1703
Jones, H. R. A., Butler, R. P., Tinney, C. G., et al. 2006, MNRAS, 369, 249
Kaib, N. A., Raymond, S. N., & Duncan, M. 2013, Natur, 493, 381
Kane, S. R. 2013, ApJ, 766, 10
Kane, S. R., Boyajian, T. S., Henry, G. W., et al. 2015, ApJ, 806, 60
Kane, S. R., Ciardi, D. R., Gelino, D. M., & von Braun, K. 2012, MNRAS, 425, 757
Kane, S. R., & Gelino, D. M. 2010, ApJ, 724, 818
Kane, S. R., & Gelino, D. M. 2011a, ApJ, 729, 74
Kane, S. R., & Gelino, D. M. 2011b, ApJ, 741, 52
Kane, S. R., & Gelino, D. M. 2012a, PASP, 124, 323
Kane, S. R., & Gelino, D. M. 2012b, MNRAS, 424, 779
Kane, S. R., Henry, G. W., Dragomir, D., et al. 2011, ApJL, 735, L41
Kane, S. R., Mahadevan, S., von Braun, K., Laughlin, G., & Ciardi, D. R. 2009, PASP, 121, 1386
Kane, S. R., & von Braun, K. 2008, ApJ, 689, 492
Latham, D. W., Mazeh, T., Stefanik, R. P., Mayor, M., & Burki, G. 1989, Natur, 339, 38
Laughlin, G., Deming, D., Langton, J., et al. 2009, Natur, 457, 562
Lewis, N. K., Knutson, H. A., Showman, A. P., et al. 2013, ApJ, 766, 95
Lodders, K., Plame, H., & Gail, H.-P. 2009, Landolt-Börnstein—Group VI Astronomy and Astrophysics Numerical Data and Functional Relationships in Science and Technology Vol. 4B, ed. J. E. Trümper, 44
Loeb, A., & Gaudi, B. S. 2003, ApJL, 588, L117
Lucy, L. B. 1967, ZA, 65, 89
Mack, C. E., Schuler, S. C., Stassun, K. G., & Norris, J. 2014, ApJ, 787, 98
Marcy, G. W., & Butler, R. P. 1996, ApJL, 464, L147
Matthews, J. M., Kuschnig, R., Guenther, D. B., et al. 2004, Natur, 430, 51
Mazeh, T. 2008, EAS, 29, 1
Meibom, S., & Mathieau, R. D. 2005, ApJ, 620, 970
Moutou, C., Hébrard, G., Bouchy, F., et al. 2009, A&A, 498, L5
Naef, D., Latham, D. W., Mayor, M., et al. 2001, A&A, 375, L27
Neves, V., Santos, N. C., Sousa, S. G., Correia, A. C. M., & Israelian, G. 2009, A&A, 497, 563
O'Toole, S. J., Tinney, C. G., Jones, H. R. A., et al. 2009, MNRAS, 392, 641
Perryman, M., Hartman, J., Bakos, G. A., & Lindegren, L. 2014, ApJ, 797, 14
Petrovich, C., Tremaine, S., & Rafikov, R. 2014, ApJ, 786, 101
Pont, F., Husnoo, N., Mazeh, T., & Fabrycky, D. 2011, MNRAS, 414, 1278
Rowe, J. F., Matthews, J. M., Seager, S., et al. 2008, ApJ, 689, 1345
Sahlmann, J., Ségransan, D., Queloz, D., et al. 2011, A&A, 525, 95
Seager, S., Richardson, L. J., Hansen, B. M. S., et al. 2005, ApJ, 632, 1122
Shporer, A., & Hu, R. 2015, AJ, 150, 112
Takeda, G., Ford, E. B., Sills, A., et al. 2007, ApJS, 168, 297
Tinney, C. G., Wittenmyer, R. A., Butler, R. P., et al. 2011, ApJ, 732, 31
Tokovinin, A., Fischer, D. A., Bonati, M., et al. 2013, PASP, 125, 1336
Valenti, J. A., Butler, R. P., & Marcy, G. W. 1995, PASP, 107, 966
Valenti, J. A., Fischer, D., Marcy, G. W., et al. 2009, ApJ, 702, 989
Valenti, J. A., & Fischer, D. A. 2005, ApJS, 159, 141
Valenti, J. A., & Piskunov, N. 1996, A&AS, 118, 595
Van Eylen, V., & Albrecht, S. 2015, ApJ, 808, 126
van Leeuwen, F. 2007a, Hipparcos, The New Reduction of the Raw Data, Vol. 350
van Leeuwen, F. 2007b, A&A, 474, 653
Vogt, S. S., Wittenmyer, R. A., Butler, R. P., et al. 2010, ApJ, 708, 1366
Walker, G., Matthews, J., Kuschnig, R., et al. 2003, PASP, 115, 1023
Wang, S. X., Wright, J. T., Cochran, W., et al. 2012, ApJ, 761, 46
Welsh, W. F., Orosz, J. A., Seager, S., et al. 2010, ApJL, 713, L145
Wittenmyer, R. A., Horner, J., Tuomi, M., et al. 2012, ApJ, 753, 169
Wittenmyer, R. A., Horner, J., Tinney, C. G., et al. 2014, ApJ, 783, 103
Wright, J. T., & Howard, A. W. 2009, ApJS, 182, 205
Zucker, S., Mazeh, T., & Alexander, T. 2007, ApJ, 670, 1326